




# Insulator-to-metal-like transition in thin films of a biological metal-organic framework

Received: 20 June 2022

Accepted: 28 April 2023

Published online: 19 May 2023

 Check for updatesPooja Sindhu<sup>1</sup>, K. S. Ananthram<sup>2</sup>, Anil Jain <sup>3,4</sup>, Kartick Tarafder <sup>2</sup> & Nirmalya Ballav <sup>1</sup> ✉

Temperature-induced insulator-to-metal transitions (IMTs) where the electrical resistivity can be altered by over tens of orders of magnitude are most often accompanied by structural phase transition in the system. Here, we demonstrate an insulator-to-metal-like transition (IMLT) at 333 K in thin films of a biological metal-organic framework (bio-MOF) which was generated upon an extended coordination of the cystine (dimer of amino acid cysteine) ligand with cupric ion (spin-1/2 system) – without appreciable change in the structure. Bio-MOFs are crystalline porous solids and a subclass of conventional MOFs where physiological functionalities of bio-molecular ligands along with the structural diversity can primarily be utilized for various biomedical applications. MOFs are usually electrical insulators (so as our expectation with bio-MOFs) and can be bestowed with reasonable electrical conductivity by the design. This discovery of electronically driven IMLT opens new opportunities for bio-MOFs, to emerge as strongly correlated reticular materials with thin film device functionalities.

Controlling charge and spin degrees of freedom in materials by external stimuli like heat, light, electric field, and the magnetic field is technologically demanding. One example is the spin-crossover phenomenon, where two or more distinct spin-states can be reversibly switched, usually varying the temperature of the system<sup>1</sup>. Another example is the resistive switching phenomenon, where the electrical resistance can be reversibly switched between a high-resistance state (insulating) and a low-resistance state (conducting) under the influence of an electric field<sup>2,3</sup>. Resistive switching is at the heart of the operation principles of non-volatile random-access computer memory devices, commonly referred to as memristors<sup>4,5</sup>. Insulators explored so far are mostly transition metal oxides (TMOs), and the switching event can be categorized in general as filamentary or interface type<sup>2,3</sup>. With an elegant demonstration of the electrically addressable memory with modest volatility<sup>6</sup>, reticular materials such as metal-organic frameworks (MOFs)<sup>7,8</sup> have recently emerged as the second-generation electrical insulators for the development of memristive devices<sup>9</sup>. Various mechanisms like thermochemical, electrochemical, valence-

charge (migration as well as re-organization), electrostatics, and ferroelectric polarization were realized with MOFs<sup>6,10–21</sup>; and additional mechanistic pathways are evolving. Specifically, the presence or absence and spatial distribution of guest molecules in the voids of MOF can significantly alter the electrical transport property<sup>22,23</sup>. Therefore, chemical constituents of the MOF and their arrangements (structural) are crucially important in achieving the resistive switching event.

The primary advantage of exploring the MOF insulators can be attributed to modular chemical design principles whereby electrical conductivity can be significantly modulated with the choice of metal ion and/or organic ligand as well as filling the pores by redox-active small molecules and/or conducting polymer moieties<sup>24</sup>. The other important factor with MOFs is the fabrication of crystalline thin films on various support substrates by simple step-by-step/layer-by-layer (LbL) technique complementing the ease of control of film thickness<sup>25</sup>. During the last two decades, various biomolecules like nucleobases, peptides, proteins, porphyrins, cyclodextrins, and small biomolecules

<sup>1</sup>Department of Chemistry, Indian Institute of Science Education and Research, Dr. Homi Bhabha Road, Pune 411 008, India. <sup>2</sup>Department of Physics, National Institute of Technology Karnataka, Surathkal, Mangalore 575 025, India. <sup>3</sup>Solid State Physics Division, Bhabha Atomic Research Centre, Mumbai 400085, India. <sup>4</sup>Homi Bhabha National Institute, Anushakti Nagar, Mumbai 400094, India. ✉e-mail: [nballav@iiserpune.ac.in](mailto:nballav@iiserpune.ac.in)

like amino acids were successfully used as organic building blocks for the generation of various types of biological MOFs<sup>26–28</sup>. It is apparent from the chemical backbones of biomolecules and the predominant ionic bonding scenario that bio-MOFs would be mostly electrical insulators, likewise conventional MOFs. In fact, the electrical transport properties of bio-MOFs are rarely explored, and so is the exploration of resistive switching as well as an insulator-to-metal transition (IMT). Herein, we report thin film (also bulk) synthesis of a bio-MOF, obtained upon reacting the cystine ligand ([SCH<sub>2</sub>CH(NH<sub>2</sub>)CO<sub>2</sub>H]<sub>2</sub>, an oxidized dimer of amino acid cysteine) with Cu(II) ion (spin-1/2), abbreviated here as Cu(Cys)<sub>2</sub> (Supplementary Figs. 1–6). Just by controlling the temperature, we could reversibly switch the resistance value across the Cu(Cys)<sub>2</sub> thin film between  $\sim 10^{11} \Omega$  at 300 K (insulating state) and  $\sim 10 \Omega$  at 333 K (conducting state) at ambient pressure with an additional hysteretic effect (Fig. 1a and Supplementary Figs. 7 and 8)—resembling the recently demonstrated electrical field-induced IMT in thin films of archetypal TMO, vanadium dioxide (VO<sub>2</sub>; spin-1/2), little above room temperature (340 K)<sup>29</sup>.

## Results

As revealed by field-emission scanning electron microscopy (FESEM) images, our  $\sim 1.2 \mu\text{m}$  thick Cu(Cys)<sub>2</sub> film, fabricated by LbL technique, was uniformly extending over hundreds of microns as well as crystalline (Fig. 1b and Supplementary Fig. 4). Cu(Cys)<sub>2</sub> thin film was realized to be highly durable under thermal stress whereby the respective resistance values at 300 and 333 K were found to be almost unaltered over ten continued cycles of heating and cooling viz. retention of the

“on-off” ratio of  $\sim 10^{10}$  (Fig. 1c). Also, resistance value at 333 K was found to be highly stable over long period of time and the time-dependent stability was successfully reproduced in the subsequent cycles (Fig. 1d). Considering the remarkable change in the resistance value ( $\sim 10^{10}$  times), such a thermally-driven phenomenon in the Cu(Cys)<sub>2</sub> thin film can be assigned to an IMT-like transition (IMLT). Estimated resistivity values for the Cu(Cys)<sub>2</sub> thin film at 300 and 333 K were found to be  $\sim 10^{10} \Omega\text{m}$  and  $\sim 10^{-1} \Omega\text{m}$ , respectively (Supplementary Fig. 7). Further, we have recorded the current–voltage (*I*–*V*) profiles for the Cu(Cys)<sub>2</sub> thin film from room temperature down to 160 K and no appreciable change in the conductance value was observed, even though the trend was similar to that of an insulator (Supplementary Fig. 9). In case of the IMT involving band-type and Mott-type insulators where the resistivity can be altered over tens of orders of magnitude are most often accompanied by structural phase transition in the system<sup>30</sup>. It is expected that for inherent Mott insulators, IMT, usually induced by temperature, should be of purely electronic origin (without structural change)<sup>31–33</sup>. However, strong Coulomb interaction over bandwidth leads to coupling of charge, spin, and lattice; and eventually, IMT (including the transition to semimetal state<sup>34,35</sup>) involving Mott insulators are also frequently associated with structural change. Notable exceptions of temperature-induced IMT in Mott insulators, without structural change, are surface-tailored layered perovskite Ca<sub>1.9</sub>Sr<sub>0.1</sub>RuO<sub>4</sub> and compositionally tuned hetero-structured VO<sub>2</sub> thin film<sup>33,36</sup>.

We have recorded X-ray diffraction (XRD) patterns on the Cu(Cys)<sub>2</sub> thin film by systematically varying the temperature from

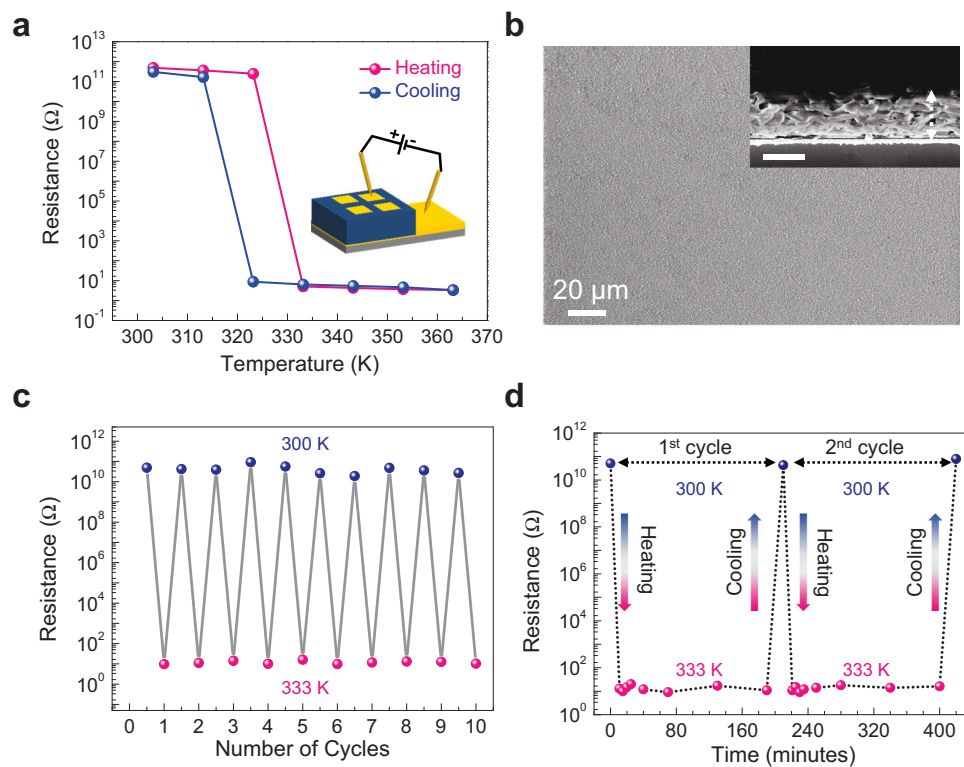


**Fig. 1 | Electrical transport property across the Cu(Cys)<sub>2</sub> thin film.**

**a** Temperature-dependent resistance values of the Cu(Cys)<sub>2</sub> thin film in the cross-plane mode during heating (pink spheres) and cooling (blue spheres) of the sample with a clearly visible hysteretic effect (inset: schematic of the transport measurement with top patterned Au contact and bottom Au substrate as electrodes). Reversible modulation of the resistance values ensured that no diffusion of Au from the contact pads across the Cu(Cys)<sub>2</sub> thin film took place during the micro-fabrication process as well during the heating-cooling cycle. **b** Surface morphology of the Cu(Cys)<sub>2</sub> thin film as revealed by FESEM image (inset: cross-plane FESEM

image with a scale bar of 1  $\mu\text{m}$  showing the thickness of the Cu(Cys)<sub>2</sub> thin film as  $\sim 1.2 \mu\text{m}$ ). **c** Cycling stability of the IMLT in the Cu(Cys)<sub>2</sub> thin film. **d** Time-dependent cycling stability: after measuring the resistance value at 300 K (0 h), the sample was heated to 333 K and kept for a few hours at 333 K; the resistance values were measured at different time intervals, and indeed, no significant change was observed (even by 10 times). Subsequently, the sample was cooled back to 300 K, and the resistance value was measured to be the same as the value at the starting point (0 h). Such behavior was successfully reproduced in the second heating-cooling cycle. Source data are provided as a Source Data file.

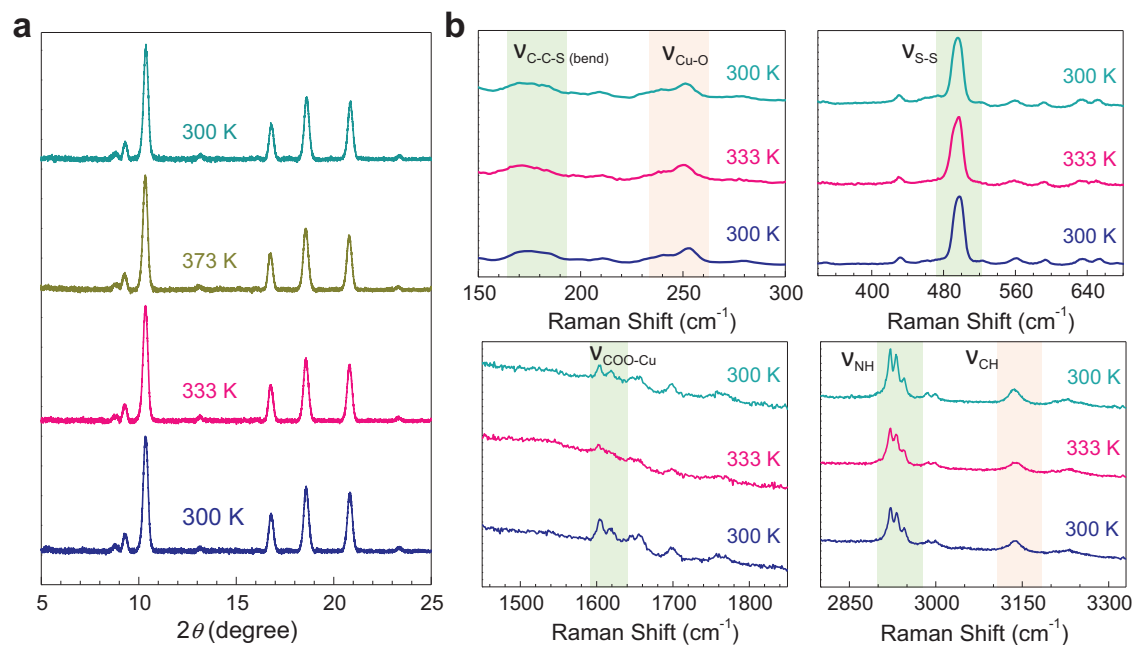


**Fig. 2 | Probing retention of structural integrity by variable temperature XRD and Raman.** **a** XRD patterns recorded on the Cu(Cys)<sub>2</sub> thin film sample at 300, 333, 373, and back to 300 K. The pattern remained almost identical across various

temperatures. **b** Raman spectra recorded on the Cu(Cys)<sub>2</sub> thin film sample at 300, at 333, and back to 300 K. Characteristic vibrational features mentioned and spectral regions are highlighted. Source data are provided as a Source Data file.

300 K up to 373 K (and back to 300 K) which could serve as the key marker to investigate any structural change in the system (Fig. 2a and Supplementary Fig. 10). Interestingly, no appreciable change in the XRD patterns could be detected during the heating and cooling cycle. Grazing-incidence XRD (GIXRD) pattern at 300 K ensured that the sharp and separated pattern was not related to any interface effect, but the material itself (Supplementary Fig. 4), and notably, similar XRD patterns were consistently observed in our earlier reports on thin films of coordination polymers. Therefore, in the course of the IMLT, structural order parameters were almost retained in the Cu(Cys)<sub>2</sub> thin film—primarily an electronic phenomenon, likewise in Ca<sub>1.9</sub>Sr<sub>0.1</sub>RuO<sub>4</sub> and VO<sub>2</sub>. To complement the temperature-dependent XRD data, we have recorded Raman spectra on the Cu(Cys)<sub>2</sub> thin film at 300, 333, and back to 300 K (Fig. 2b and Supplementary Fig. 11). Characteristic vibrational signatures were found to be unaltered at different temperatures; specifically, C–C–S bending mode (175 cm<sup>-1</sup>), Cu–O (240 cm<sup>-1</sup>), S–S stretching mode (496 cm<sup>-1</sup>), COO–Cu stretching mode (1603 cm<sup>-1</sup>), C–H (-CH<sub>2</sub>-) stretching modes (2921 cm<sup>-1</sup>, 2932 cm<sup>-1</sup>, and 2945 cm<sup>-1</sup>), and N–H (-NH<sub>2</sub>) stretching mode (3136 cm<sup>-1</sup>)<sup>37,38</sup>. Therefore, Raman spectra confirmed that IMLT in the Cu(Cys)<sub>2</sub> thin film did not accompany any change in the coordination environment, viz., chemical bonding integrity was retained in the system. One relevant example is the intertwining of redox chemistry and IMT in a MOF induced by oxygen (O<sub>2</sub>) adsorption–desorption chemistry leading to a profound change in the electronic structure throughout the material<sup>39</sup>. Another example is the insulator-to-proton-conductor transition in a dense MOF upon exposure to humidity<sup>40</sup>. Also, solvation-desolvation with water molecules was observed to significantly impact the electrical conductivity of a one-dimensional MOF<sup>41</sup>. However, these examples dealt with a change in the chemical integrity of the systems resembling the chemically-driven IMT in oxides<sup>42</sup> and unlike the temperature-induced IMLT presented here with a bio-MOF. Notably, in the spectral range of 3000–3800 cm<sup>-1</sup>, no signature of water adsorption-desorption could be detected in our temperature-dependent Raman spectra on the Cu(Cys)<sub>2</sub> thin film; specifically peaks at 3215 and 3371 cm<sup>-1</sup> (respective symmetric and asymmetric OH stretch modes of hydrogen-bonded

water) as well as a peak at 3683 cm<sup>-1</sup> (water adsorbed in the pores)<sup>43</sup> (Supplementary Fig. 11).

One-dimensional (1D) zig-zag chains can be visualized in the simulated crystal structure of our Cu(Cys)<sub>2</sub> system [Cu(C<sub>3</sub>H<sub>5</sub>NO<sub>2</sub>S)<sub>2</sub>] with four coordination around the Cu(II) ion (two N and two O) and these 1D chains are interconnected by H-bonding giving rise to three-dimensional (3D) framework structure (Fig. 3). Initial geometry of the Cu(Cys)<sub>2</sub> unit cell was constructed from the reported Zn(Cys)<sub>2</sub> [Zn(C<sub>3</sub>H<sub>5</sub>NO<sub>2</sub>S)<sub>2</sub>] crystal structure<sup>44</sup>, in which Zn(II) ions were replaced with Cu(II) ions and then the Cu(Cys)<sub>2</sub> energy-optimised ground state geometry was obtained by performing the density functional theory (DFT) calculations. The energy-optimized structure was subjected to Rietveld refinement of the XRD pattern of the Cu(Cys)<sub>2</sub> thin film<sup>45</sup>. Preferred orientation was determined by looking at the XRD peak intensities and was applied during the Rietveld refinement<sup>46</sup>, whereby a reasonably fair match between the experimental and calculated XRD patterns was achieved (Supplementary Fig. 12). To complement the XRD data, high-resolution transmission electron microscopy (HRTEM) analysis was performed on an extracted sample from the Cu(Cys)<sub>2</sub> thin film, and HRTEM image along with the corresponding fast-Fourier transformed (FFT) and inverse fast-Fourier transformed (IFFT) patterns clearly revealed existence of highly periodic 1D zig-zag chains (Fig. 3)<sup>47,48</sup>.

Barring structural phase transition, such a dramatic change in the resistance value in the Cu(Cys)<sub>2</sub> system can be associated with the contact interface. In earlier work, we have shown thermally driven resistive switching in Cu-TCNQ and Ag-TCNQ (TCNQ = 7,7,8,8-tetracyanoquinodimethane) which was attributed to the alternation of a Schottky barrier at the contact interface, i.e., primarily an interface effect<sup>49</sup>. Specifically, the change in the in-plane resistance value in the Ag-TCNQ thin film at 400 K varied from 10<sup>4</sup> fold to 10<sup>6</sup> fold in comparison to the value at 300 K, depending on the type of contact electrode. As for the Cu-TCNQ thin film, the enhancement factor was observed to be 10<sup>4</sup>. Later on, upon increasing the temperature from 300 to 400 K, both in-plane and cross-plane modes, we realized a significant change in the resistance value for the thin film of Cu-TCNQ; and, interestingly, no change in the resistance value for the thin film of

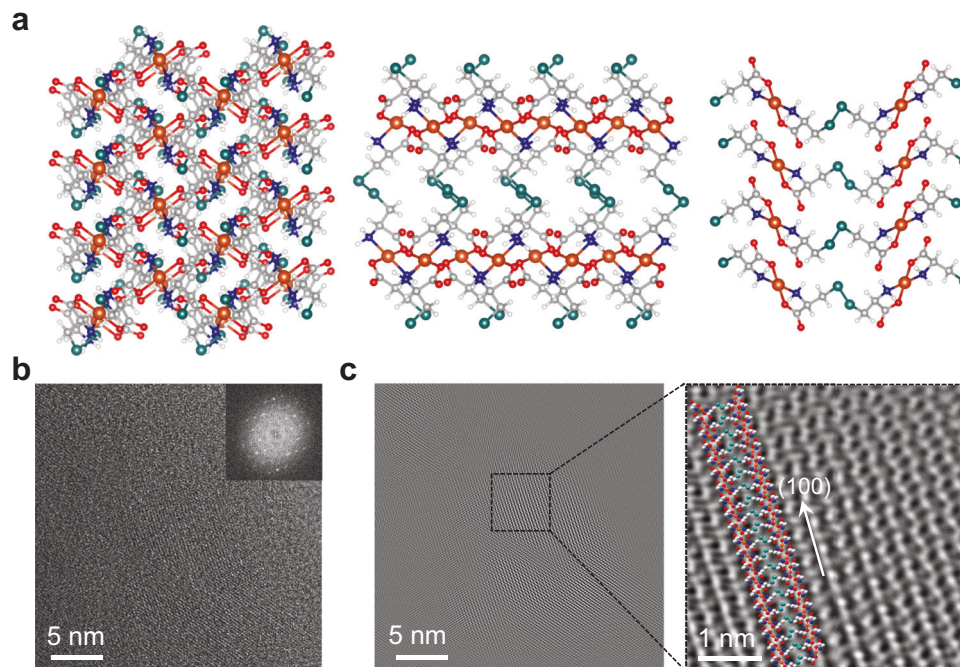


**Fig. 3 | Proposed structure of the Cu(Cys)<sub>2</sub> system.** **a** Structural view from the *a*-axis (left panel), *b*-axis (middle panel), and *c*-axis (right panel) where carbon, hydrogen, nitrogen, oxygen, sulfur, and copper atoms are represented by gray, white, blue, red, dark cyan and orange colors, respectively. **b** HRTEM image of the

Cu(Cys)<sub>2</sub> sample (inset: corresponding fast-Fourier transform (FFT) image). **c** Inverse fast-Fourier transform (IFFT) pattern extracted from the HRTEM image showing a good overlap with the crystal structure along (100) direction.

Cu-BTC (BTC = 1,3,5-benzenetricarboxylate)<sup>50</sup>. Therefore, it is the intrinsic property of the material, for example, Mott-type (Cu-TCNQ) or band-type (Cu-BTC) insulator<sup>46,51</sup>, which played a more important role than the influence of the interfaces. In the present study, successful capture of the IMLT for the Cu(Cys)<sub>2</sub> thin film (thickness ~1.2 μm) in both cross-plane and in-plane modes (consistent change in the resistance by 10<sup>10</sup> fold) clearly endorses that it is not primarily an interface effect. Also, in-plane *I-V* profiles on the Cu(Cys)<sub>2</sub> thin film with various metallic contacts having different work function values (Au, W, and Eutectic-GaIn)<sup>49</sup> revealed mainly Ohmic-type electrical transport, both at 300 and 333 K; and the change in the resistance by 10<sup>10</sup> fold was consistent (Supplementary Figs. 13 and 14). Even upon performing in-plane *I-V* measurements with patterned Pt pads (having relatively higher work function value of ~6.3 eV) on top of the Cu(Cys)<sub>2</sub> thin film gave the same results (Supplementary Fig. 15).

The robustness of the IMLT phenomenon motivated us to test the device functionality, and accordingly, we have employed photolithography followed by sputtering Au contact pads on the Cu(Cys)<sub>2</sub> thin film (Fig. 4a). Well-defined patterns with various channel lengths (Fig. 4b) as well as sizes of the Au contact pads (Fig. 4c) can be clearly visualized in the optical and FESEM images. After the microfabrication process involving multi-steps, the structural integrity of the Cu(Cys)<sub>2</sub> thin film was fully retained, as was reflected in the FESEM images, XRD patterns, and the Raman spectra (Supplementary Fig. 16). The IMLT captured in the cross-plane mode (Fig. 1a) was also successfully captured in our patterned sample in the in-plane mode. Upon systematic variation of the channel length (50, 100, 150, and 200 μm) while keeping the contact area same (50 × 50 μm<sup>2</sup>), no appreciable change in the resistance value was observed, both at 300 K as well as 333 K (Fig. 4d and Supplementary Fig. 17). Also, systematically varying the contact pad area (50 × 50 μm<sup>2</sup>, 100 × 100 μm<sup>2</sup>, 150 × 150 μm<sup>2</sup> and 200 × 200 μm<sup>2</sup>) while keeping the channel length same (50 μm), the resistance values did not change noticeably, both at 300 and 333 K (Fig. 4e and Supplementary Fig. 18). To strengthen the IMLT effect, we have fabricated Cu(Cys)<sub>2</sub> thin films of different thickness values

(~750 nm, ~980 nm, and ~1.5 μm) and upon changing the temperature of the samples from 300 to 333 K, an increase in the conductance value by 10<sup>10</sup> fold was consistently observed (Supplementary Figs. 19 and 20). Such robustness in the *I-V* profiles along with the reversibility of the IMLT phenomenon, further ruled out the possibility of diffusion of Au from the contact pads into the Cu(Cys)<sub>2</sub> thin film. Therefore, keeping in mind the intricate role of the electronic structure of the interface, our various complementary electrical transport measurements highlighting the consistent linear *I-V* profiles within ±0.5 V, in both in-plane and cross-plane modes, endorsed IMLT phenomenon as a unique property of the Cu(Cys)<sub>2</sub> thin film.

## Discussion

In order to get mechanistic insights into the origin of such an electronically driven IMLT phenomenon, DFT calculations combined with molecular dynamics (MD) simulations were performed on the Cu(Cys)<sub>2</sub> system at three different temperatures (0, 280, and 350 K). The total density of states (DOS) plots obtained at 0, 280, and 350 K are presented in Fig. 5. An important observation in the DOS plot at 0 K was the appearance of a discrete state around Fermi energy ( $E_F$ , ±0.25 eV) which was mainly originating from the Cu atoms, as identified in the atom-projected partial density of states (PDOS) plot (Supplementary Fig. 21). Also, the discrete state was populated by approximately one electron density, residing mostly on the  $t_{2g}$  set of the 3d orbitals of Cu (Supplementary Fig. 22); and the energy gap between the valence band (VB) minimum and the discrete state was found to be ~1.0 eV. Therefore, Cu(Cys)<sub>2</sub> can be ascribed as a Mott-type insulator<sup>30,52</sup>. Upon increasing the temperature from 0 to 280 K, the width of the discrete state around  $E_F$  was increased (±0.5 eV), and with a significant contribution from S atoms (Supplementary Fig. 21), the VB minimum shifted towards  $E_F$ , thereby reducing the energy gap. Remarkably, at 350 K, the discrete state at  $E_F$  was merged with the VB and a metal-like continuous density of states was realized viz. overlapping of the Cu-based states via the S-based state (Supplementary Fig. 21). Additionally, total charge density plots (Supplementary

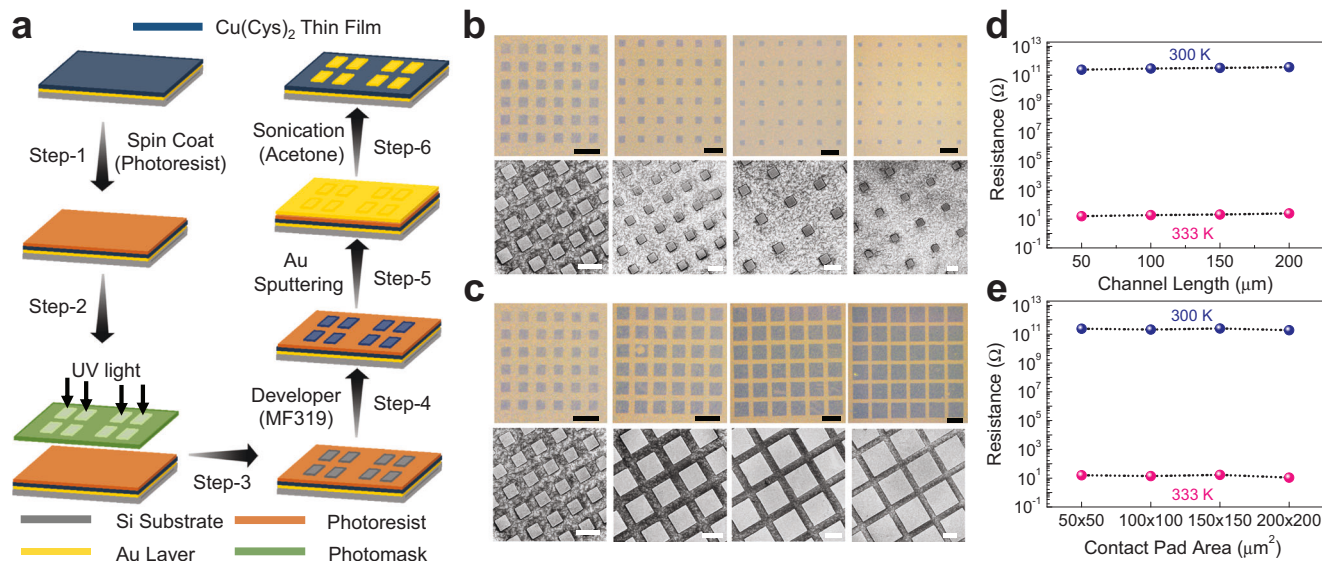


**Fig. 4 | Testing device functionality of the Cu(Cys)<sub>2</sub> thin film.** **a** Schematic of the fabrication of patterned Au pads on top of the Cu(Cys)<sub>2</sub> thin film by photolithography. **b** Optical (top panels; scale bars represent 200 μm length) and FESEM (bottom panels; scale bars represent 100 μm length) images of the 50, 100, 150, and 200 μm channels (left to right) with Au contact pads on the top of Cu(Cys)<sub>2</sub> thin film. Scale bars are provided. **c** Optical (top panels; scale bars represent 200 μm

length) and FESEM (bottom panels; scale bars represent 100 μm length) images of the 50 × 50 μm<sup>2</sup>, 100 × 100 μm<sup>2</sup>, 150 × 150 μm<sup>2</sup> and 200 × 200 μm<sup>2</sup> (left to right) Au contact pads. **d** Plot of resistance values versus and channel length at 300 K (blue spheres) and 333 K (pink spheres). **e** Plot of resistance values versus and contact pad area at 300 K (blue spheres) and 333 K (pink spheres). Source data are provided as a Source Data file.

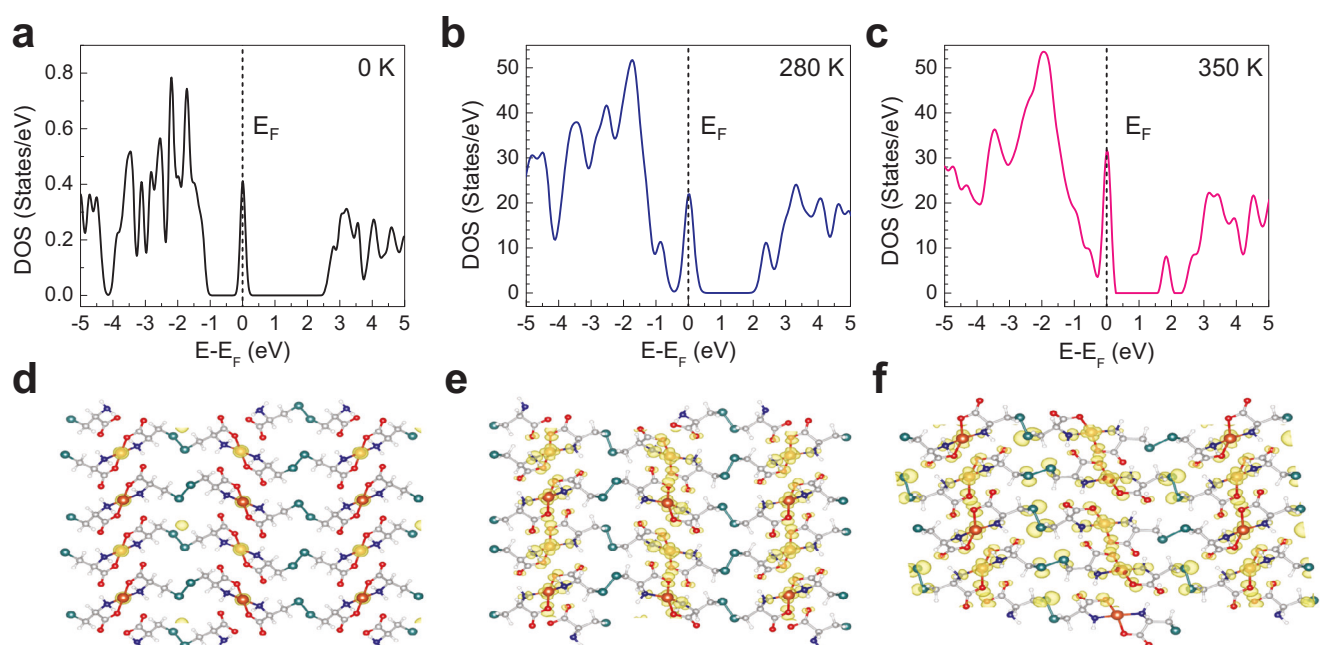


**Fig. 5 | Unravelling mechanistic insights of the IMLT phenomenon.** Total density of state (DOS) plots for the Cu(Cys)<sub>2</sub> structure at 0 K (**a**), 280 K (**b**), and 350 K (**c**) ( $E_F$  is marked by the dotted black lines). Partial charge density plots for the Cu(Cys)<sub>2</sub> structure around  $E_F$  ( $\pm 0.5$  eV) at 0 K (**d**), 280 K (**e**), and 350 K (**f**) where carbon,

hydrogen, nitrogen, oxygen, sulfur, and copper atoms are represented by grey, white, blue, red, dark cyan and orange colors, respectively; and electron accumulation is represented by yellow isosurface. Source data are provided as a Source Data file.

Fig. 23) and partial charge density plots (Fig. 5) were carefully examined and Bader charge analysis<sup>39,46,53</sup> was carried out to understand the distribution of charge on various atoms at different temperatures which showed that S atom released and Cu atom accumulated charges at higher temperatures (Supplementary Table 1) so that the respective electronic band structures were affected by the overall charge redistribution across the high-symmetry points (Supplementary Fig. 24). Thus, IMLT in our Cu(Cys)<sub>2</sub> system can be attributed to be due to the

onset of an electronic coupling primarily involving 3*d* and 3*p* orbitals of Cu and S atoms, respectively (possibly, via 2*p* orbitals of N atoms)—without any appreciable change in the structure and/or coordination. Notably, earlier studies revealed that infinite chains and planes of (-M-S)<sub>∞</sub> in MOF structures (so-called “through-bond” approach)<sup>24,54,55</sup>, specifically the (-Cu-S)<sub>∞</sub> linkage, could enable efficient charge-transport leading to high-electrical conductivity in the systems. The present study is clearly unraveling the innovative ‘through-space’

avenue (-Cu---S)<sub>∞</sub> as well as stimulates the usage of Mott-type insulator Cu(Cys)<sub>2</sub> in neuromorphic device applications<sup>52</sup>. Finally, we have theoretically calculated electrical conductivity values for the Cu(Cys)<sub>2</sub> system at different temperatures, which qualitatively complemented our experimental observation on the IMLT phenomenon, specifically the trend, and certainly encourage further investigations (Supplementary Fig. 25 and Table 2).

In summary, we have presented a thermally driven and fully reversible IMT-like transition in a thin film of Cu(Cys)<sub>2</sub> at ambient pressure and a little above room temperature. The transition was achieved without a noticeable change in the structure and assigned to be of mainly electronic origin, viz., a charge cross-over phenomenon. Successful capturing of the IMLT in the photo-lithographically patterned sample, along with the robust current-voltage characteristics, ensured the device application possibilities of the Cu(Cys)<sub>2</sub> thin film. This work is anticipated to provide a new platform for studying the coupling of charge, spin, and lattice degrees of freedom in correlated biological reticular materials. Thermally-driven supercurrent in biological MOFs is also envisioned.

## Methods

### Chemicals

Copper acetate [Cu(OAc)<sub>2</sub>·H<sub>2</sub>O], L-Cysteine, 11-Merceptoundecanoic acid (MUDA), and Au(111) substrate (100 nm Au coated Si wafer) were purchased from Sigma-Aldrich and ethanol from Merck and used without any further purification except Au(111) substrate.

### Functionalization of Au substrate

Au substrate was cleaned by dipping into Piranha solution (H<sub>2</sub>SO<sub>4</sub> (95–98%)/H<sub>2</sub>O<sub>2</sub> (30%); v/v 3:1) for 30 min (note: proper safety care must be taken) and washed with Milli-Q water followed by ethanol and then dried under the stream of N<sub>2</sub> gas. Subsequently, the Au substrate was functionalized with a carboxy-terminated (-COOH) self-assembled monolayer (SAM) by dipping into the 1 mM MUDA solution in ethanol/acetic acid (v/v 9:1) for 48 h followed by washing with ethanol and dried with N<sub>2</sub> gas<sup>56,57</sup>.

### Fabrication of Cu(Cys)<sub>2</sub> thin film

MUDA functionalized Au substrate was immersed in 1 mM ethanolic solution of Cu(OAc)<sub>2</sub>·H<sub>2</sub>O kept at 330 K for 30 min, followed by washing with ethanol and subsequently in 2 mM Cysteine solution in ethanol–water (1:1) mixture kept at 330 K for 30 min (washed with ethanol in between followed by drying with a stream of N<sub>2</sub> gas) to complete one LbL cycle<sup>50</sup>. Thirty cycles of LbL were performed to get uniform Cu(Cys)<sub>2</sub> thin film (thickness values were estimated to be ~1.2 μm). Employing the same experimental conditions, thin films of Cu(Cys)<sub>2</sub> with thickness values of ~750 nm, ~980 nm, and ~1.5 μm were also fabricated, corresponding to LbL growth of 20 cycles, 25 cycles, and 35 cycles, respectively.

### Synthesis of Cu(Cys)<sub>2</sub> powder

Cu(OAc)<sub>2</sub>·H<sub>2</sub>O (1 mM) and Cysteine (2 mM) solutions were prepared in ethanol and ethanol–water (1:1) mixture, respectively, and mixed together in a round bottom flask. The solution was kept at 330 K with constant stirring for the next 3 days. A sky-blue colored powder was collected after centrifugation with water and ethanol three times alternatively.

### Characterizations

The surface morphologies of thin film and bulk performed by Zeiss Ultra Plus FESEM. Contact angle measurements were measured using Holmarc's Contact Angle Meter. Out-of-plane XRD data were recorded at room temperature and high temperature using a Bruker D8 Advance diffractometer using Cu K<sub>α</sub> radiation (λ = 1.5406 Å). Raman spectra (λ<sub>exc</sub> = 632.8 nm) were recorded at Raman microscope (LabRAM HR,

HoribaJobinYvon) with a 50× objective lens, and the spectral resolution of the system is ~1 cm<sup>-1</sup>. FTIR spectra were collected in the range of 400–4000 cm<sup>-1</sup> with a resolution of ~4 cm<sup>-1</sup> using KBr pellets (NICOLET 6700 spectrophotometer). High-resolution XPS spectra were recorded by using a Thermo Fisher Scientific ESCALAB Xi+ for both bulk and thin film, and a hand-book<sup>58</sup> was referred for the assignments of various photoemission signals. ESR was recorded using JES - FA200 ESR Spectrometer with an X band on the bulk sample. Gas adsorption and desorption isotherms were collected at 77 K for N<sub>2</sub> gas on the BelSorpmax instrument (pore size distribution was obtained from the standard H–K model). HRTEM images were recorded on drop casted samples (methanolic dispersion) over a 200 mesh Cu grid using JEOL USA JEM-2200 FS Transmission Electron Microscope (scratched sample in case of thin film). TGA profiles were recorded using Perkin-Elmer thermal analyzer STA 6000 model. Electrical transport measurements (current–voltage, *I*-*V* profiles) on various thin film samples were carried out using a Keithley 4200 SCS Parameter Analyser system attached to an Everbeing probe station with eutectic gallium indium (EGaIn) alloy, tungsten tip, Au and Pt pads and direct Au tip as the contact electrodes, in two-probe configuration. During the electrical transport measurements at ambient pressure, relative humidity (RH) values at 300 and 333 K were noted to be ~46% and ~38%, respectively.

### Photolithography

It was performed by LW405 Laser writer, followed by the deposition of Au by using LTE sputter 080. A standardized procedure<sup>49</sup> was adopted as follows: Step-1: Spin coating of photoresist (SI813; ~0.2 to ~0.3 ml; thickness ~2 μm) on the Cu(Cys)<sub>2</sub> thin film; Step-2: a patterned mask was applied to block the UV light, and only unmasked regions of the material were exposed to the UV light; Step-3: the exposed photosensitive material is degraded by the UV light; Step-4: the degraded material is dissolved in developer (MF319) solution; Step-5: Au (~100 nm) was sputtered on the patterned thin film; and Step-6: patterned thin film was sonicated in acetone for 1–2 min to dissolve the photoresist and resulted into the well-defined Au pads on the Cu(Cys)<sub>2</sub> thin film.

### Computational studies

The unit cell of the Cu(Cys)<sub>2</sub> system was modeled by considering experimentally obtained data on the Zn(Cys)<sub>2</sub> system<sup>44</sup> (CCDC 971360), where Zn metal ions were replaced with Cu ions using an open-source molecular builder and visualization tool Avogadro<sup>59</sup>. The geometrical optimizations and the extraction of electronic structure information were achieved by using the Vienna Ab-initio Simulation Package (VASP) with projector augmented wave method<sup>60</sup>. The Perdew–Burke–Ernzerhof functional of generalized gradient approximation<sup>61</sup> was employed as exchange–correlation functions to estimate the accurate DOS and band structure<sup>62</sup> of the Cu(Cys)<sub>2</sub> system. The conjugate gradient method was used to obtain the energy-optimized structure, and the optimization process was carried out until the interatomic forces in the system were reduced to 0.001 eV/Å. The Brillouin zone integration is performed using a 5 × 5 × 3, Monkhorst–Pack grid. To study the temperature-dependent electronic structure and calculate the electronic conductivity, MD simulations were carried out at different temperatures using Parrinello and Rahman method as implemented in VASP. In our simulation process, we have used Langevin dynamics<sup>63–65</sup> for the isobaric–isothermal ensemble where the Brillouin zone was sampled at the Gamma point 1 × 1 × 1 and a PAW basis-set with energy cut-off of 600 eV was considered. To equilibrate the sample at a particular temperature, we used 1.0 fs per step and simulated the sample for a minimum of 150,000 MD steps. Simulated mean temperatures achieved at thermal equilibrium were 279.16 K and 350.61 K for 280 K and 350 K, respectively. The thermally equilibrated samples were further used to study the electrical conductivity of the system at different temperatures. Conductivity

calculations were performed by using the Boltzmann transport method implemented in BOLTZWANN code<sup>66</sup> distributed with Wannier90 package<sup>67</sup>. In this method, the semi-classical Boltzmann transport equations were solved for the periodic infinite system under the constant relaxation-time approximation, where the band energies and band derivatives were obtained via Wannier interpolations. We have used plane wave (PW) results obtained from VASP to construct the maximally localized Wannier functions, which were interpolated accurately to calculate transport quantities on a coarse k-point reciprocal space grid. In the present calculation, highly dense  $40 \times 40 \times 40$  k-mesh was used for the interpolation in constructing tight-binding Hamiltonian matrix elements. All individual snapshots at different temperatures obtained from MD simulations were considered as the initial configuration. And maximally localized Wannier functions were derived by choosing the individual projection. Electrical conductivity was calculated for a chemical potential equal to 0 eV by minimizing the real space spread of individual Wannier functions. Bader charge analysis<sup>53</sup> was performed using Henkelman's Group program<sup>68–70</sup>.

### Crystal structure analysis

Structural characterization of the thin film was carried out by performing the Rietveld analysis of the XRD data using the FullProf program<sup>45</sup>. Our analysis shows that crystallites are preferentially oriented toward three directions which makes a real refinement using traditional software packages such as FullProf and GSAS difficult because, in these packages, it is onerous to include more than one preferred orientation direction. The initial crystal structural parameters for the refinement were taken from the Zn(Cys)<sub>2</sub> system (CCDC 971360)<sup>44</sup>, with Zn(II) ions replaced by Cu(II) ions and energy-optimized by DFT calculations. In the present case, the diffraction pattern was simulated by considering the three preferred orientations (110), (−101), (01-1) with lattice parameters,  $a = 19.999(3) \text{ \AA}$ ,  $b = 9.434(2) \text{ \AA}$ ,  $c = 5.484(1) \text{ \AA}$ ,  $\alpha = \beta = \gamma = 90^\circ$ . To account for the spectrum shifting, variation along the longer  $a$ -axis was expected due to the strain in thin films or the existence of a defect state during the initial cycles of the LbL growth at solid–liquid interface. Therefore, contraction along  $a$ -axis ( $a = 18.980 \text{ \AA}$ ) was considered during the simulation along with the aforementioned cell parameters, with preferred orientation along (100), with the maximum fraction of 5%, which led to the good match of refined diffraction pattern to the experimental diffraction pattern.

### Reporting summary

Further information on research design is available in the Nature Portfolio Reporting Summary linked to this article.

### Data availability

All data supporting the findings of this study are available within this article and its Supplementary Information, as well as from the corresponding author upon request. Source data are provided in this paper.

### References

1. Kahn, O. & Martinez, C. J. Spin-transition polymers: from molecular materials toward memory devices. *Science* **279**, 44–48 (1998).
2. Sawa, A. Resistive switching in transition metal oxides. *Mater. Today* **11**, 28–36 (2008).
3. Waser, R. & Aono, M. Nanoionics-based resistive switching memories. *Nat. Mater.* **6**, 833–840 (2007).
4. Chua, L. O. The fourth element. *Proc. IEEE* **100**, 1920–1927 (2012).
5. Wang, Z. et al. Resistive switching materials for information processing. *Nat. Rev. Mater.* **5**, 173–195 (2020).
6. Yoon, S. M., Warren, S. C. & Grzybowski, B. A. Storage of electrical information in metal–organic-framework memristors. *Angew. Chem. Int. Ed.* **53**, 4437–4441 (2014).
7. Zhou, H.-C., Long, J. R. & Yaghi, O. M. Introduction to metal–organic frameworks. *Chem. Rev.* **112**, 673–674 (2012).
8. Yaghi, O. M. et al. Reticular synthesis and the design of new materials. *Nature* **423**, 705–714 (2003).
9. Oh, J. & Yoon, S. M. Resistive memory devices based on reticular materials for electrical information storage. *ACS Appl. Mater. Interfaces* **13**, 56777–56792 (2021).
10. Pan, L. et al. A resistance-switchable and ferroelectric metal–organic framework. *J. Am. Chem. Soc.* **136**, 17477–17483 (2014).
11. Yao, Z. et al. Simultaneous implementation of resistive switching and rectifying effects in a metal–organic framework with switched hydrogen bond pathway. *Sci. Adv.* **5**, eaaw4515 (2019).
12. Park, M.-J. & Lee, J.-S. Zeolitic-imidazole framework thin film-based flexible resistive switching memory. *RSC Adv.* **7**, 21045–21049 (2017).
13. Huang, X. et al. Coating two-dimensional nanomaterials with metal–organic frameworks. *ACS Nano* **8**, 8695–8701 (2014).
14. Zhao, L. et al. Nonvolatile electrical bistability behaviors observed in Au/Ag nanoparticle-embedded MOFs and switching mechanisms. *ACS Appl. Mater. Interfaces* **11**, 47073–47082 (2019).
15. Ding, G. et al. 2D metal–organic framework nanosheets with time-dependent and multilevel memristive switching. *Adv. Func. Mater.* **29**, 1806637 (2019).
16. Pan, L. et al. Metal–organic framework nanofilm for mechanically flexible information storage applications. *Adv. Func. Mater.* **25**, 2677–2685 (2015).
17. Wang, Z. et al. Resistive switching nanodevices based on metal–organic frameworks. *ChemNanoMat* **2**, 67–73 (2016).
18. Ohara, H. et al. Layer-by-layer growth control of metal–organic framework thin films assembled on polymer films. *ACS Appl. Mater. Interfaces* **12**, 50784–50792 (2020).
19. Yi, X. et al. Intrinsically stretchable resistive switching memory enabled by combining a liquid metal-based soft electrode and a metal–organic framework insulator. *Adv. Electron. Mater.* **5**, 1800655 (2019).
20. He, Y. et al. Encapsulating halometallates into 3-D lanthanide-iodogen frameworks: controllable emissions, reversible thermochromism, photocurrent responses, and electrical bistability behaviors. *Inorg. Chem.* **58**, 13862–13880 (2019).
21. Moreno-Moreno, M. et al. One-pot preparation of mechanically robust, transparent, highly conductive, and memristive metal–organic ultrathin film. *ACS Nano* **12**, 10171–10177 (2018).
22. Liu, Y. et al. Alcohol-mediated resistance-switching behavior in metal–organic framework-based electronic devices. *Angew. Chem. Int. Ed.* **55**, 8884–8888 (2016).
23. Albano, L. G. S. et al. Ambipolar resistive switching in an ultrathin surface-supported metal–organic framework vertical heterojunction. *Nano Lett.* **20**, 1080–1088 (2020).
24. Xie, L. S., Skorupskii, G. & Dincă, M. Electrically conductive metal–organic frameworks. *Chem. Rev.* **120**, 8536–8580 (2020).
25. Liu, J. & Wöll, C. Surface-supported metal–organic framework thin films: fabrication methods, applications, and challenges. *Chem. Soc. Rev.* **46**, 5730–5770 (2017).
26. McKinlay, A. C. et al. BioMOFs: metal–organic frameworks for biological and medical applications. *Angew. Chem. Int. Ed.* **49**, 6260–6266 (2010).
27. Imaz, I. et al. Metal–biomolecule frameworks (MBioFs). *Chem. Commun.* **47**, 7287–7302 (2011).
28. Cai, H., Huang, Y.-L. & Li, D. Biological metal–organic frameworks: structures, host–guest chemistry and bio-applications. *Coord. Chem. Rev.* **378**, 207–221 (2019).
29. Valle, J. D. et al. Spatiotemporal characterization of the field-induced insulator-to-metal transition. *Science* **373**, 907–911 (2021).
30. Imada, M., Fujimori, A. & Tokura, Y. Metal-insulator transitions. *Rev. Mod. Phys.* **70**, 1039–1263 (1998).

31. Mott, N. F. The basis of the electron theory of metals, with special reference to the transition metals. *Proc. Phys. Soc. Lond. Sect. A* **62**, 416 (1949).
32. Mott, N. F. *Metal-Insulator Transitions* (Taylor & Francis, London, 1974).
33. Moore, R. G. et al. A surface-tailored, purely electronic, Mott metal-to-insulator transition. *Science* **318**, 615–619 (2007).
34. Sow, C. et al. Current-induced strong diamagnetism in the Mott insulator  $\text{Ca}_2\text{RuO}_4$ . *Science* **358**, 1084–1087 (2017).
35. Bertinshaw, J. et al. Unique crystal structure of  $\text{Ca}_2\text{RuO}_4$  in the current stabilized semimetallic state. *Phys. Rev. Lett.* **123**, 137204 (2019).
36. Lee, D. et al. Isostructural metal-insulator transition in  $\text{VO}_2$ . *Science* **362**, 1037–1040 (2018).
37. Diaz Fleming, G. et al. Experimental and theoretical Raman and surface-enhanced Raman scattering study of cysteine. *J. Raman Spec.* **40**, 632–638 (2009).
38. Minkov, V. S., Goryainov, S. V., Boldyreva, E. V. & Görbitz, C. H. Raman study of pressure-induced phase transitions in crystals of orthorhombic and monoclinic polymorphs of L-cysteine: dynamics of the side chain. *J. Raman Spec.* **41**, 1748–1758 (2010).
39. Maximoff, S. N. & Smit, B. Redox chemistry and metal-insulator transitions intertwined in a nano-porous material. *Nat. Commun.* **5**, 4032 (2014).
40. Tominaka, S., Coudert, F.-X., Dao, T. D., Nagao, T. & Cheetham, A. K. Insulator-to-proton-conductor transition in a dense metal-organic framework. *J. Am. Chem. Soc.* **137**, 6428–6431 (2015).
41. Kon, K. et al. Electron-conductive metal-organic framework,  $\text{Fe}(\text{d}(\text{h}(\text{b}(\text{q}))(\text{d}(\text{h}(\text{b}(\text{q}))) = 2,5\text{-Dihydroxy-1,4-benzoquinone})$ : coexistence of microporosity and solid-state redox activity. *ACS Appl. Mater. Interfaces* **13**, 38188–38193 (2021).
42. Nagarajan, L. et al. A chemically driven insulator-metal transition in non-stoichiometric and amorphous gallium oxide. *Nat. Mater.* **7**, 391–398 (2008).
43. Tan, K. et al. Water interactions in metal organic frameworks. *CrystEngComm* **17**, 247–260 (2015).
44. Ferrer, P., da Silva, I., Rubio-Zuazo, J. & Castro, G. R. Synthesis and crystal structure of the novel metal organic framework  $\text{Zn}(\text{C}_3\text{H}_5\text{NO}_2\text{S})_2$ . *Powder Diffr.* **29**, 366–370 (2014).
45. Rodríguez-Carvajal, J. Recent advances in magnetic structure determination by neutron powder diffraction. *Phys. B Condens. Matter* **192**, 55–69 (1993).
46. Sindhu, P., Ananthram, K. S., Jain, A., Tarafder, K. & Ballav, N. Charge-transfer interface of insulating metal-organic frameworks with metallic conduction. *Nat. Commun.* **13**, 7665 (2022).
47. Peng, X. et al. Observation of formation and local structures of metal-organic layers via complementary electron microscopy techniques. *Nat. Commun.* **13**, 5197 (2022).
48. Tong, L. et al. Atomically unveiling the structure-activity relationship of biomacromolecule-metal-organic frameworks symbiotic crystal. *Nat. Commun.* **13**, 951 (2022).
49. Rana, S., Prasoon, A., Jha, P. K., Prathamshetti, A. & Ballav, N. Thermally driven resistive switching in solution-processable thin films of coordination polymers. *J. Phys. Chem. Lett.* **8**, 5008–5014 (2017).
50. Sindhu, P., Prasoon, A., Rana, S. & Ballav, N. Emergent interface in heterostructured thin films of  $\text{Cu}(\text{II})$  and  $\text{Cu}(\text{I})$  coordination polymers. *J. Phys. Chem. Lett.* **11**, 6242–6248 (2020).
51. Dolgoplova, E. A. et al. Electronic properties of bimetallic metal-organic frameworks (MOFs): tailoring the density of electronic states through MOF modularity. *J. Am. Chem. Soc.* **139**, 5201–5209 (2017).
52. Zhou, Y. & Ramanathan, S. Mott memory and neuromorphic devices. *Proc. IEEE* **103**, 1289–1310 (2015).
53. Bader, R. F. W. *Atoms in Molecules: A Quantum Theory*. (Clarendon Press, 1994).
54. Sun, L., Miyakai, T., Seki, S. & Dincă, M.  $\text{Mn}_2(2,5\text{-disulfhydrylbenzene-1,4-dicarboxylate})$ : a microporous metal-organic framework with infinite  $(-\text{Mn}-\text{S}-)_\infty$  chains and high intrinsic charge mobility. *J. Am. Chem. Soc.* **135**, 8185–8188 (2013).
55. Pathak, A. et al. Integration of a  $(-\text{Cu}-\text{S}-)_n$  plane in a metal-organic framework affords high electrical conductivity. *Nat. Commun.* **10**, 1721 (2019).
56. Arnold, R., Azzam, W., Terfort, A. & Wöll, C. Preparation, modification, and crystallinity of aliphatic and aromatic carboxylic acid terminated self-assembled monolayers. *Langmuir* **18**, 3980–3992 (2002).
57. Rana, S., Rajendra, R., Dhara, B., Jha, P. K. & Ballav, N. Highly Hydrophobic and chemically rectifiable surface-anchored metal-organic framework thin-film devices. *Adv. Mater. Interfaces* **3**, 1500738 (2016).
58. Moulder, J. F., Stickle, W. F., Sobol, P. E. & Bomben, K. D. *Handbook of X-Ray Photoelectron Spectroscopy: A Reference Book of Standard Spectra for Identification of XPS Data*. (Perkin-Elmer, 1992).
59. Hanwell, M. D. et al. Avogadro: an advanced semantic chemical editor, visualization, and analysis platform. *J. Cheminform* **4**, 17 (2012).
60. Kresse, G. & Furthmüller, J. Efficient iterative schemes for ab initio total-energy calculations using a plane-wave basis set. *Phys. Rev. B* **54**, 11169–11186 (1996).
61. Perdew, J. P., Burke, K. & Ernzerhof, M. Generalized gradient approximation made simple. *Phys. Rev. Lett.* **77**, 3865–3868 (1996).
62. Hinuma, Y., Pizzi, G., Kumagai, Y., Oba, F. & Tanaka, I. Band structure diagram paths based on crystallography. *Comput. Mater. Sci.* **128**, 140–184 (2017).
63. Allen, M. P. & Tildesley, D. J. *Computer Simulation of Liquids*. (Oxford University Press, New York, 1991).
64. Hoover, W. G., Ladd, A. J. C. & Moran, B. High-strain-rate plastic flow studied via nonequilibrium molecular dynamics. *Phys. Rev. Lett.* **48**, 1818–1820 (1982).
65. Evans, D. J. Computer “experiment” for nonlinear thermodynamics of Couette flow. *J. Chem. Phys.* **78**, 3297–3302 (1983).
66. Pizzi, G., Volja, D., Kozinsky, B., Fornari, M. & Marzari, N. BoltzWann: a code for the evaluation of thermoelectric and electronic transport properties with a maximally-localized Wannier functions basis. *Comput. Phys. Commun.* **185**, 422–429 (2014).
67. Mostofi, A. A. et al. wannier90: a tool for obtaining maximally-localised Wannier functions. *Comput. Phys. Commun.* **178**, 685–699 (2008).
68. Henkelman, G., Arnaldsson, A. & Jónsson, H. A fast and robust algorithm for Bader decomposition of charge density. *Comput. Mater. Sci.* **36**, 354–360 (2006).
69. Sanville, E., Kenny, S. D., Smith, R. & Henkelman, G. Improved grid-based algorithm for Bader charge allocation. *J. Comput. Chem.* **28**, 899–908 (2007).
70. Tang, W., Sanville, E. & Henkelman, G. A grid-based Bader analysis algorithm without lattice bias. *J. Phys.* **21**, 084204 (2009).

## Acknowledgements

Financial support from Science and Engineering Research Board, India, Project No. CRG/2020/001804 and IISER Pune, India, are acknowledged. P.S. thanks to CSIR (India) for Research Fellowship and Mr. Vikash Kumar for useful discussions.

## Author contributions

P.S. prepared samples and performed the experiments under the guidance of N.B. A.K.S. performed DFT calculations under the guidance of K.T. A.J. performed the structural analysis, including Rietveld



refinement. N.B. conceived and supervised the research project and wrote the paper with input from the co-authors.

### Competing interests

The authors declare no competing interests.

### Additional information

**Supplementary information** The online version contains supplementary material available at <https://doi.org/10.1038/s41467-023-38434-4>.

**Correspondence** and requests for materials should be addressed to Nirmalya Ballav.

**Peer review information** *Nature Communications* thanks Christian Serre and the other anonymous reviewer(s) for their contribution to the peer review of this work.

**Reprints and permissions information** is available at <http://www.nature.com/reprints>

**Publisher's note** Springer Nature remains neutral with regard to jurisdictional claims in published maps and institutional affiliations.

**Open Access** This article is licensed under a Creative Commons Attribution 4.0 International License, which permits use, sharing, adaptation, distribution and reproduction in any medium or format, as long as you give appropriate credit to the original author(s) and the source, provide a link to the Creative Commons license, and indicate if changes were made. The images or other third party material in this article are included in the article's Creative Commons license, unless indicated otherwise in a credit line to the material. If material is not included in the article's Creative Commons license and your intended use is not permitted by statutory regulation or exceeds the permitted use, you will need to obtain permission directly from the copyright holder. To view a copy of this license, visit <http://creativecommons.org/licenses/by/4.0/>.

© The Author(s) 2023